



Numerical Studies of Magnetic Reconnection and Heating Mechanisms for the Ellerman Bomb

Mingyu Liu^{1,2}, Lei Ni^{1,2,3}, Guan-Chong Cheng^{1,2}, Udo Ziegler⁴, and Jun Lin^{1,2,3}
¹Yunnan Observatories, Chinese Academy of Sciences, Kunming 650216, China; leini@ynao.ac.cn
²University of Chinese Academy of Sciences, Beijing 100049, China
³Center for Astronomical Mega-Science, Chinese Academy of Sciences, Beijing 100101, China
⁴Astrophysikalisches Institut Potsdam D-14482 Potsdam, Germany

Received 2022 October 28; revised 2022 December 26; accepted 2022 December 28; published 2023 February 28

Abstract

An Ellerman Bomb (EB) is a kind of small scale reconnection event, which is ubiquitously formed in the upper photosphere or the lower chromosphere. The low temperature ($<10,000$ K) and high density ($\sim 10^{19}-10^{22}$) plasma there makes the magnetic reconnection process strongly influenced by partially ionized effects and radiative cooling. This work studies the high β magnetic reconnection near the solar temperature minimum region based on high-resolution 2.5D magnetohydrodynamics simulations. The time-dependent ionization degree of hydrogen and helium are included to realize more realistic diffusivities, viscosity and radiative cooling in simulations. Numerical results show that the reconnection rate is smaller than 0.01 and decreases with time during the early quasi-steady stage, then sharply increases to a value above 0.05 in the later stage as the plasmoid instability takes place. Both the large value of η_{en} (magnetic diffusion caused by the electron-neutral collision) and the plasmoid instability contribute to the fast magnetic reconnection in the EB-like event. The interactions and coalescence of plasmoids strongly enhance the local compression heating effect, which becomes the dominant mechanism for heating in EBs after plasmoid instability appears. However, the Joule heating contributed by η_{en} can play a major role to heat plasmas when the magnetic reconnection in EBs is during the quasi-steady stage with smaller temperature increases. The results also show that the radiative cooling effect suppresses the temperature increase to a reasonable range, and increases the reconnection rate and generation of thermal energy.

Key words: magnetic reconnection – magnetohydrodynamics (MHD) – Sun: chromosphere – Sun: activity

1. Introduction

The interaction among the neutrals and ionized plasmas that affects magnetic reconnection is one of the major scientific challenges in understanding explosive phenomena in magnetized plasmas in the universe (e.g., Ni et al. 2020; Ji et al. 2022). The relatively cold and dense environment in the low solar atmosphere provides a natural laboratory that helps us to understand magnetic reconnection in partially ionized plasmas (Wang 1995). As the observational techniques develop, a growing number of small scale reconnection events have been observed, such as Ellerman Bombs (EBs) (e.g., Ellerman 1917; Ding et al. 1998; Georgoulis et al. 2002), ultraviolet bursts (e.g., Peter et al. 2014; Tian et al. 2016; Chen et al. 2019), spicules and chromospheric jets (e.g., dePontieu et al. 2007; Samanta et al. 2019; Shen 2021; Schmieder et al. 2022), nanoflares and campfires (e.g., Parnell & Jupp 2000; Song et al. 2020; Berghmans et al. 2021; Chen et al. 2021; Joshi et al. 2021), and some other explosive events (e.g., Huang et al. 2019; Rast et al. 2021; Xue et al. 2021).

Ellerman (1917) discovered an EB for the first time by analyzing $H\alpha$ spectral line profiles in an active spot-group,

where a sudden brightening in a very narrow band extending a few angstroms on either side of the spectral line was observed. EBs usually show elongated structures at $H\alpha - 0.8 \text{ \AA}$ (e.g., Georgoulis et al. 2002; Pariat et al. 2007), and can possibly be composed of fine structures (Hashimoto et al. 2010). Plenty of observations affirm that they also have strong emissions in Ca II lines (e.g., Fang et al. 2006; Pariat et al. 2007; Vissers et al. 2013, 2015). Recent high-quality observations in $H\beta$ indicate that EBs are ubiquitous in the quiet Sun and appear everywhere (Joshi & Ruppe van der Voort 2022). The size of an EB is about $1''$ and the typical lifetime is a few minutes (e.g., Georgoulis et al. 2002; Pariat et al. 2007). Statistical studies of their energy spectra show that the released energy in an EB is between 10^{25} and 10^{28} erg (e.g., Georgoulis et al. 2002; Fang et al. 2006). The temperature increase in EBs is about 600–3000 K according to the results based on semi-empirical models and numerous spectral analyses (e.g., Georgoulis et al. 2002; Fang et al. 2006; Hong et al. 2017).

Magnetic reconnection is believed to be the main mechanism that accounts for an EB. When EBs happen, the strength of the measured magnetic fields at the solar surface of the

corresponding reconnection region is about a few hundred Gauss (e.g., Pariat et al. 2004, 2007; Li et al. 2015). However, the reconnection diffusion region in EBs is still poorly understood because of the limited resolutions of the existing solar telescopes. The multi-wavelength spectral studies and radiative hydrodynamic simulations demonstrate that EBs always occur in the upper photosphere or the lower chromosphere (e.g., Hong et al. 2017, 2021) where the plasma density is around 10^{19} – 10^{22} cm^{-3} and it is weakly ionized according to the C7 solar atmosphere model (Avrett & Loeser 2008). Therefore, the strong radiative cooling and partially ionized effects have to be considered when we study magnetic reconnection in this region.

Previous single-fluid two-dimensional (2D) magnetohydrodynamics (MHD) simulations have studied magnetic reconnection between anti-parallel magnetic fields in the low solar atmosphere (Chen et al. 2001; Xu et al. 2011), where the temperature increase and duplicated $\text{H}\alpha$ and Ca II line profiles can be qualitatively compared with observations. Magnetic reconnections between the U-shaped magnetic fields triggered by Parker instability have also been shown to occur in both 2D and three-dimensional (3D) MHD simulations (Isobe et al. 2007; Archontis & Hood 2009), which are consistent with the scenario that EBs are usually observed in the regions with serpentine magnetic field lines (Pariat et al. 2004). Recent 3D radiation MHD simulations studied magnetic reconnection between the emerging magnetic field and the background magnetic field below the temperature minimum region (TMR) (Danilovic et al. 2017; Danilovic 2017), and the synthesized images in the $\text{H}\alpha$ wing seen from different angles are similar to the flame-like structures observed, and the synthetic magnetograms obtained from $\text{Fe I } 6301 \text{ \AA}$ are also consistent with observations. However, we should point out that all these previous MHD simulations about modeling EBs in the stratified solar atmosphere usually focus on comparisons with observations, and the heating mechanisms and small scale physics in the reconnection region were not examined.

The theoretical and numerical studies about magnetic reconnection in partially ionized plasmas indicate that the ambipolar diffusion caused by the decoupling of ions and neutrals (Brandenburg & Zweibel 1994), the ion recombination effect (Leake et al. 2012, 2013) and radiative cooling (Uzdensky et al. 2010) can accelerate reconnection when the guide field vanishes. Both single-fluid and multi-fluid MHD simulations show that turbulent reconnection mediated by plasmoids also appears in the low solar atmosphere (Leake et al. 2012, 2013; Murphy & Lukin 2015; Ni et al. 2015, 2016; Ni & Lukin 2018; Singh et al. 2019; Murtas et al. 2021, 2022), and plasmoid instability can lead to fast magnetic reconnection (Ni et al. 2015; Ni & Lukin 2018), especially in the case of low β (Ni & Lukin 2018). Which of these mechanisms govern fast

magnetic reconnection in an EB is still an open question. Previous simulations also indicate that Joule heating is very important for converting magnetic energy into heat (Ni et al. 2016) in such a dense plasma. The heating caused by ambipolar diffusion can be ignored in a low β reconnection process around the solar TMR (Ni et al. 2021, 2022), but it might play a role in a high β reconnection event such as an EB (Chae & Litvinenko 2021). When plasmoid instability appears in the reconnection current sheet, many small scale slow-mode and fast-mode shocks appear inside the plasmoid (Ni et al. 2015, 2016), which can also heat plasmas in the reconnection region. The strong horizontal flows at the solar surface are usually observed during the EB formation process. Recent 3D MHD simulations demonstrate that these horizontal flows caused by external forces can drive the reconnection process and cause compression heating in EBs (Cheng et al. 2021). Nevertheless, the heating mechanism in EBs still needs more precise simulations to verify.

In this work, we study reconnection and the heating mechanism in EBs based on single-fluid MHD simulations. The MHD models have been improved by including both hydrogen and helium, and the time-dependent ionization degree of these two elements, which makes the magnetic diffusion caused by electron-neutral collision, the ambipolar diffusion and the radiative cooling effect more realistic than those in previous simulations (Ni et al. 2015, 2016). The numerical methods are described in Section 2. We present the numerical results in Section 3. Discussions about fast reconnection and heating mechanisms in EB are provided in Section 4. We give our conclusions and outlooks in Section 5.

2. Numerical Methods

2.1. MHD Equations

In this work, we use the optimized single-fluid MHD code NIRVANA (Ziegler 2008, 2011) to perform the 2.5D MHD simulations. All the five components including hydrogen atoms, helium atoms, electrons, and ions contributed by ionized hydrogen and helium are considered to be well coupled as a single fluid. The solved MHD equations are the same as those in the recent work by Ni et al. (2022):

$$\frac{\partial \rho}{\partial t} = -\nabla \cdot (\rho \mathbf{v}), \quad (1)$$

$$\frac{\partial(\rho \mathbf{v})}{\partial t} = -\nabla \cdot \left[\rho \mathbf{v} \mathbf{v} + \left(p + \frac{1}{2\mu_0} |\mathbf{B}|^2 \right) \mathbf{I} - \frac{1}{\mu_0} \mathbf{B} \mathbf{B} \right] + \nabla \cdot \tau_S, \quad (2)$$

Table 1
Collision Cross Sections, the Unit is m^2

σ_{e-nH}	σ_{e-nHe}	σ_{iH-nH}	σ_{iH-nHe}	σ_{iHe-nH}	$\sigma_{iHe-nHe}$
2×10^{-19}	$\frac{2}{3} \times 10^{-19}$	1.5×10^{-18}	$\frac{1.5}{\sqrt{3}} \times 10^{-18}$	$\frac{1.5}{\sqrt{3}} \times 10^{-18}$	$\frac{1.5}{\sqrt{3}} \times 10^{-18}$

$$\begin{aligned} \frac{\partial e}{\partial t} = & -\nabla \cdot \left[\left(e + p + \frac{1}{2\mu_0} |\mathbf{B}|^2 \right) \mathbf{v} \right] \\ & + \nabla \cdot \left[\frac{1}{\mu_0} (\mathbf{v} \cdot \mathbf{B}) \mathbf{B} \right] \\ & + \nabla \cdot \left[\mathbf{v} \cdot \tau_S + \frac{\eta}{\mu_0} \mathbf{B} \times (\nabla \times \mathbf{B}) \right] \\ & - \nabla \cdot \left[\frac{1}{\mu_0} \mathbf{B} \times \mathbf{E}_{AD} \right] + Q_{\text{rad}} + H, \end{aligned} \quad (3)$$

$$\frac{\partial \mathbf{B}}{\partial t} = \nabla \times (\mathbf{v} \times \mathbf{B} - \eta \nabla \times \mathbf{B} + \mathbf{E}_{AD}), \quad (4)$$

$$e = \frac{p}{\gamma - 1} + \frac{1}{2} \rho |\mathbf{v}|^2 + \frac{1}{2\mu_0} |\mathbf{B}|^2, \quad (5)$$

$$p = \frac{(1.1 + Y_{iH} + 0.1Y_{iHe})\rho}{1.4m_i} k_B T. \quad (6)$$

The variables ρ , \mathbf{v} , \mathbf{B} , p , T , e , Y_{iH} and Y_{iHe} are the mass density, fluid velocity, magnetic field, thermal pressure, temperature, total energy density, and ionization fractions of hydrogen and helium, respectively. \mathbf{E}_{AD} is the ambipolar diffusion electric field, τ_S is the stress tensor, and Q_{rad} and H are the radiative cooling and heating terms respectively, which will be more detailedly described in the next subsections. The magnetic diffusivity η is contributed by both electron-ion collision (η_{ei}) and electron-neutral collision (η_{en}). The constant values of $m_i = 1.66057 \times 10^{-27}$ kg, $k_B = 1.3806 \times 10^{-23}$ J K $^{-1}$, $\mu_0 = 4\pi \times 10^{-7}$ V s A $^{-1}$ m $^{-1}$ and $\gamma = 5/3$ are the mass of a proton, Boltzmann constant, magnetic permeability coefficient and ratio of specific heats, respectively. The International System of Units (SI) are applied in the simulations.

We study magnetic reconnection around the solar TMR, where the ion-neutral collision frequency is about 10^8 s $^{-1}$, and the ion inertial length and ion-neutral collision mean free path are about 1 m and 100 m (e.g., Leake et al. 2013; Ni & Lukin 2018), respectively. Therefore, it is reasonable to use such a single-fluid model when we study an EB-like event with a length scale of 200 km. However, we should also point out that the single-fluid model will eventually break down when the reconnection length scale decreases down to the ion-neutral collision mean free path. In this work, the effects of neutrals are embodied by the magnetic diffusion caused by electron-neutral collision and ambipolar diffusion. The number density of the total helium is assumed to be 10% of the total hydrogen. We

only consider the primary ionization of helium, and it is reasonable in our low temperature simulations. Since the current sheet in our simulations is assumed to be parallel to the solar surface, we ignore gravity and the initial plasma density is taken as a constant.

2.2. Diffusions and Viscosity

The high plasma density in EBs causes strong collisions between different kinds of particles. In this subsection, we will introduce the magnetic diffusion, ambipolar diffusion and viscosity applied in this work. The magnetic diffusion is contributed by both electron-neutral collision and electron-ion collision, while the ambipolar diffusion mainly relates to the ion-neutral collisions, and the viscosity is mainly caused by ion-ion collisions and neutral-neutral collisions. The different cross sections used to calculate the diffusions and viscosity are listed in Table 1; their values are given according to the previous work (Barata & Conde 2010; Vranjes & Krstic 2013), here σ_{e-nH} , σ_{e-nHe} , σ_{iH-nH} , σ_{iH-nHe} , σ_{iHe-nH} , $\sigma_{iHe-nHe}$ and σ_{nH-nH} are the collision cross sections of electron-neutral hydrogen collision, electron-neutral helium collision, ion hydrogen-neutral hydrogen collision, ion hydrogen-neutral helium collision, ion helium-neutral hydrogen collision, ion helium-neutral helium collision and neutral hydrogen-neutral hydrogen collision, respectively.

The magnetic diffusivity η contributed by two different kinds of collisions is expressed as

$$\eta = \eta_{ei} + \eta_{en}. \quad (7)$$

According to the recent work Ni et al. (2022), the final expressions are as below:

$$\eta_{ei} \simeq 1.0246 \times 10^8 \Lambda T^{-1.5}, \quad (8)$$

$$\eta_{en} \simeq 0.0351 \sqrt{T} \frac{\left[\frac{0.1}{3} (1 - Y_{iHe}) + (1 - Y_{iH}) \right]}{Y_{iH} + 0.1Y_{iHe}}, \quad (9)$$

where the unit for η_{ei} and η_{en} is $\text{m}^2 \text{s}^{-1}$. The expression for the Coulomb logarithm Λ is written as

$$\Lambda = 23.4 - 1.15 \log_{10} n_e + 3.45 \log_{10} T, \quad (10)$$

where $n_e = \rho(Y_{iH} + 0.1Y_{iHe})/(1.4m_i)$ is the number density of electrons, expressed in cgs units (cm^{-3}), and T is expressed in eV.

The ambipolar diffusion electric field \mathbf{E}_{AD} in the energy equation, Equation (3), and induction equation, Equation (4), is

given by

$$\mathbf{E}_{AD} = \frac{1}{\mu_0} \eta_{AD} [(\nabla \times \mathbf{B}) \times \mathbf{B}] \times \mathbf{B}, \quad (11)$$

where η_{AD} is the ambipolar diffusion coefficient. The formula of η_{AD} is as below (Ni et al. 2020, 2022)

$$\eta_{AD} = \frac{(\rho_n/\rho)^2}{\rho_i \nu_{in} + \rho_e \nu_{en}}, \quad (12)$$

where the unit of η_{AD} is $\text{m}^3 \text{s kg}^{-1}$. Since the plasmas are composed of hydrogen and helium, we can obtain:

$$\rho_n/\rho = \frac{0.4(1 - Y_{\text{He}}) + (1 - Y_{\text{H}})}{1.4}, \quad (13)$$

$$\begin{aligned} \rho_i \nu_{in} = & \rho_{\text{H}} n_{\text{H}} \sqrt{\frac{8k_B T}{\pi m_i/2}} \sigma_{i\text{H}-\text{nH}} \\ & + \rho_{\text{H}} n_{\text{He}} \sqrt{\frac{8k_B T}{\pi 4m_i/5}} \sigma_{i\text{H}-\text{nHe}} \\ & + \rho_{\text{He}} n_{\text{H}} \sqrt{\frac{8k_B T}{\pi 4m_i/5}} \sigma_{i\text{He}-\text{nH}} \\ & + \rho_{\text{He}} n_{\text{He}} \sqrt{\frac{8k_B T}{\pi 2m_i}} \sigma_{i\text{He}-\text{nHe}}, \end{aligned} \quad (14)$$

where $\rho_{\text{H}} = \rho Y_{\text{H}}/1.4$ is the ionized hydrogen density and $\rho_{\text{He}} = 0.4\rho Y_{\text{He}}/1.4$ is the ionized helium density. According to the previous inference (Ni et al. 2022), the electron collision part $\rho_e \nu_{en}$ can be ignored.

The stress tensor in the momentum equation, Equation (2), and the energy equation, Equation (3), is given as

$$\tau_S = \xi \left[\nabla \mathbf{v} + (\nabla \mathbf{v})^T - \frac{2}{3} (\nabla \cdot \mathbf{v}) \mathbf{I} \right], \quad (15)$$

where ξ is the dynamic viscosity coefficient and its unit is $\text{kg m}^{-1} \text{s}^{-1}$. The expression for the dynamic viscosity can be simply written as below (Ni et al. 2022)

$$\xi = 10^{-7} \sqrt{T}. \quad (16)$$

The detailed derivation process of these diffusions and viscosity can be found in the recent work about magnetic reconnection in ultraviolet bursts (Ni et al. 2022). The ionization degrees of hydrogen and helium are based on the RADYN test atmosphere results by solving the radiative transfer equations (Carlsson & Leenaarts 2012), which vary with plasma temperature as plotted in Figure 1(a). The ionization degree of helium is a simple exponential function of temperature, $Y_{\text{He}} = 1 - 10^{0.325571 - 0.00005967T}$. According to this expression, the value of Y_{He} will become negative if the temperature is lower than 5413 K. Therefore, we assume $Y_{\text{He}} = 0.00010084814$ when $T < 5413$ K. The curve of Y_{He} (as displayed in Figure 1) is a good fit down to 50% ionization at $T = 10^4$ K.

2.3. Radiative Cooling Models

The radiative cooling effect is very strong in an EB, which cannot be ignored when we study magnetic reconnection in this region. As we know, the photosphere can be considered to be in local thermodynamic equilibrium (LTE) and the chromosphere is in a non-LTE state, which is much more complicated when we try to solve the radiative transfer equations in this region (Rutten 2003). Gan & Fang (1990) derived a simple radiative cooling expression according to the observational experiences, which can roughly measure the radiative cooling effect in the low solar atmosphere. The chromospheric radiative energy balance is dominated by a small number of strong lines from neutral hydrogen, singly ionized calcium and singly ionized magnesium (Vernazza et al. 1981). Carlsson & Leenaarts (2012) provided a simple radiative cooling model based on the three lines, which is considered as the most accurate simple radiative cooling for the chromosphere, especially for the upper chromosphere. The reconnection region we study is around the solar TMR. We cannot tell which model is more accurate for this region. Therefore, we simulate different cases with the two different radiative cooling models and compare the results.

As clearly described in the recent work Ni et al. (2022), the first radiative cooling model (Carlsson & Leenaarts 2012) is written as below

$$\begin{aligned} Q_{\text{rad1}} = & - \sum_{X=\text{H,Mg,Ca}} L_{Xm}(T) E_{Xm}(\tau) \\ & \times \frac{N_{Xm}}{N_X}(T) A_X \frac{N_{\text{H}}}{\rho} n_e \rho, \end{aligned} \quad (17)$$

where $L_{Xm}(T)$ is the optically thin radiative loss function varying with temperature T , per electron and per particle of element X in ionization state m , $E_{Xm}(\tau)$ is the escape probability as a function of the depth parameter τ , $\frac{N_{Xm}}{N_X}(T)$ is the fraction of element X that is in ionization state m , A_X is the abundance of element X and $\frac{N_{\text{H}}}{\rho} = 4.407 \times 10^{23} \text{ g}^{-1}$ is the number of hydrogen particles per gram of chromospheric material. The units in Carlsson & Leenaarts (2012) are CGS and we transform the units into SI in this work. When such a radiative cooling model is applied, it will be turned on when the temperature is larger than 4434 K, otherwise $Q_{\text{rad1}} = 0$. We set the heating term $H = 0$ when Q_{rad1} is applied to the simulation.

The second radiative cooling model (Gan & Fang 1990) is expressed as below

$$Q_{\text{rad2}} = -1.547 \times 10^{-42} n_e n_{\text{H}} \alpha T^{1.5}, \quad (18)$$

where n_{H} is the number density of the total hydrogen, and the altitude dependent parameter $\alpha = 1.805 \times 10^{-4}$ at TMR. When Q_{rad2} is applied, we set the initial heating term $H = 1.547 \times 10^{-42} n_{e0} n_{\text{H}0} \alpha T_0^{1.5}$, where T_0 is the initial temperature, and n_{e0} and $n_{\text{H}0}$ are the initial electron and total

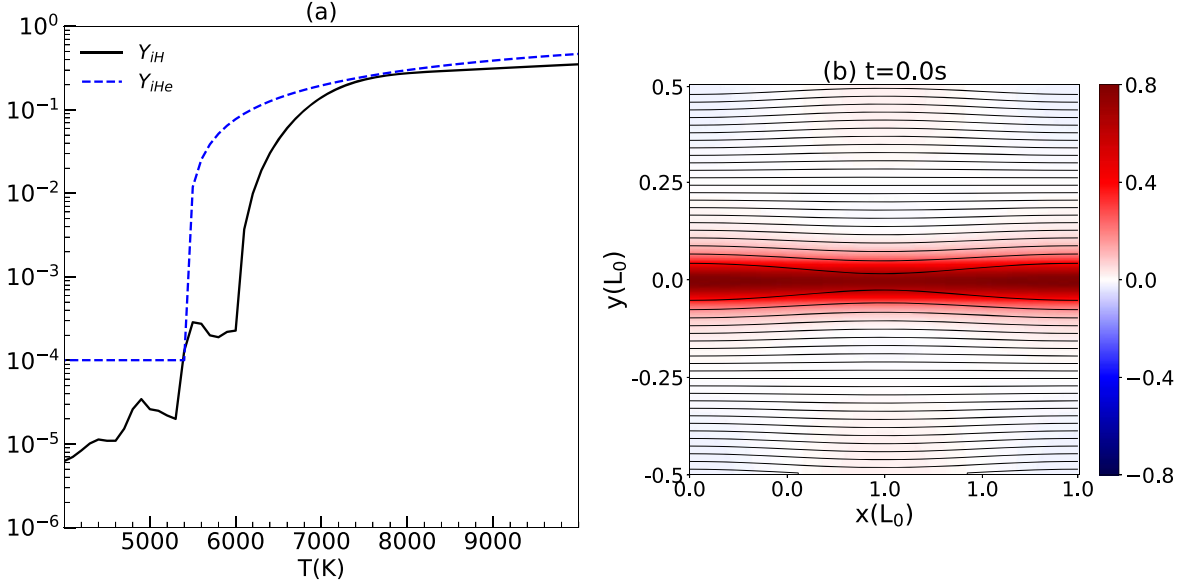


Figure 1. (a) Temperature-dependent ionization fractions of hydrogen (Y_{iH}) and helium (Y_{iHe}). (b) Field lines and current density J_z (background color) in the whole simulation domain for Case III at $t = 0$ s.

hydrogen number densities, respectively. Such a heating term is turned off when $t > 0$. This initial heating term is included to make $Q_{\text{rad}} + H = 0$ at the beginning to avoid possible artificial effects in the simulation.

2.4. Initial Setups

The simulation length scale $L_0 = 200$ km, which is comparable with the length scale of an EB. The 2D simulation domain is $0 \leq x \leq L_0$ and $-0.5L_0 \leq y \leq 0.5L_0$, and open boundary conditions are applied in both directions. According to the solar atmosphere model, we assume the initial temperature $T_0 = 4400$ K and the initial total plasma density $\rho_0 = 1.66057 \times 10^{-6}$ kg m $^{-3}$, which are the typical values around TMR. The horizontal force-free Harris sheet is applied as the initial equilibrium magnetic fields:

$$B_{x0} = -b_0 \tanh[y/(0.05L_0)], \quad (19)$$

$$B_{y0} = 0, \quad (20)$$

$$B_{z0} = b_0 / \cosh[y/(0.05L_0)], \quad (21)$$

where $b_0 = 0.01$ T. Therefore, the initial Alfvén velocity $v_{A0} = b_0 / \sqrt{\mu_0 \rho_0} = 6922$ m s $^{-1}$, the initial plasma pressure $p_0 = n_0 k_B T_0 = 47.7$ Pa and the initial plasma β is $\beta_0 = p_0 / (b_0^2 / 2\mu_0) = 1.20$, which are similar to the initial setups for studying a high β magnetic reconnection in the previous work (Ni et al. 2016).

The small perturbations for both magnetic field and velocity at the beginning are given as below:

$$b_{x1} = -b_{\text{pert}} \sin \left[\frac{2\pi(y + 0.5L_0)}{L_0} \right] \cos \left[\frac{2\pi(x + 0.5L_0)}{L_0} \right], \quad (22)$$

$$b_{y1} = b_{\text{pert}} \cos \left[\frac{2\pi(y + 0.5L_0)}{L_0} \right] \sin \left[\frac{2\pi(x + 0.5L_0)}{L_0} \right], \quad (23)$$

$$v_{y1} = v_{\text{pert}} \sin \left(\pi \frac{y}{L_0} \right) \cdot \frac{\text{random}_n}{\text{Max}(|\text{random}_n|)}, \quad (24)$$

where b_{pert} and v_{pert} are small fractions of b_0 and v_{A0} respectively, and random_n is the random noise function in the simulation code.

In order to study the effects of radiative cooling, different diffusions, initial perturbations and resolutions on magnetic reconnection around the solar TMR, we have tested many different cases. In this paper, we will show the results of seven cases, and the differences among these cases are listed in Table 2. The adaptive mesh refinement (AMR) level means the highest level of mesh refinement applied in the simulations. We can see that the only difference between Cases I, II and III is the radiative cooling model. We will compare the results from these three cases to study the effect of radiative cooling on magnetic reconnection. The only difference between Cases III, IV and V is the different diffusion terms included in these cases. The resolution in Case VI is much lower than that in the other cases, which makes the numerical diffusion dominate

Table 2
Differences Among Seven Simulation Cases

	Radiative Cooling	Magnetic Diffusion	Ambipolar Diffusion	Initial Grid	AMR Level	Smallest Grid Size	b_{pert}	v_{pert}
Case I	NO	$\eta_{\text{ei}} + \eta_{\text{en}}$	ON	192×192	8	4.07 m	$0.05b_0$	$0.005v_{A0}$
Case II	$Q_{\text{rad}2}$	$\eta_{\text{ei}} + \eta_{\text{en}}$	ON	192×192	8	4.07 m	$0.05b_0$	$0.005v_{A0}$
Case III	$Q_{\text{rad}1}$	$\eta_{\text{ei}} + \eta_{\text{en}}$	ON	192×192	8	4.07 m	$0.05b_0$	$0.005v_{A0}$
Case IV	$Q_{\text{rad}1}$	η_{ei}	OFF	192×192	8	4.07 m	$0.05b_0$	$0.005v_{A0}$
Case V	$Q_{\text{rad}1}$	$\eta_{\text{ei}} + \eta_{\text{en}}$	OFF	192×192	8	4.07 m	$0.05b_0$	$0.005v_{A0}$
Case VI	$Q_{\text{rad}1}$	$\eta_{\text{ei}} + \eta_{\text{en}}$	ON	384×384	0	520.83 m	$0.05b_0$	$0.005v_{A0}$
Case VII	$Q_{\text{rad}1}$	$\eta_{\text{ei}} + \eta_{\text{en}}$	ON	192×192	8	4.07 m	$0.01b_0$	$0.005v_{A0}$

over the physical diffusions in this case. Compared with the other cases, a much smaller initial perturbation of magnetic field is applied in Case VII.

3. Numerical Results

3.1. Results with Different Radiative Cooling Models

In order to investigate the effects of radiative cooling on the magnetic reconnection process in EBs, we will detailedly describe and compare the results in Cases I, II and III in this subsection. The radiative cooling term is turned off in Case I, while $Q_{\text{rad}2}$ and $Q_{\text{rad}1}$ are separately included in the energy equation in Case II and Case III.

The evolutions of the current sheet in different cases are shown in Figure 2. The 2D distributions of the temperature and plasma density at three different times are presented in this figure, in which the two different background colors in half of the upper and lower panels represent the temperature and density, respectively. The time evolutions of the maximum temperature T_{max} , the maximum velocity in the x -direction $v_{x\text{max}}$ and the reconnection rate γ in the three cases are presented in Figure 3. The reconnection rate is calculated as: $\gamma = v_{y\text{-aver}}/v_{A\text{-aver}}$, where $v_{y\text{-aver}}$ is the average velocity in the y -direction and $v_{A\text{-aver}}$ is the average Alfvén velocity inside a small region around the main reconnection X-point; the red boxes in Figure 2 are these small regions for calculating the reconnection rate.

The initial Harris sheet always becomes thinner and thinner, and then breaks down to form the plasmoid instability at around $t = 37$ s in all the three cases. These plasmoids collide and coalesce to form bigger and bigger ones. As discussed in the previous papers Ni et al. (2016, 2022), many slow and fast mode shocks are formed inside the plasmoids during the collision process, which can also be identified in Figure 2. As demonstrated in Figures 2 and 3, the evolutions of all the variables are very similar in the three cases before plasmoid instability appears.

After that, the radiative cooling strongly affects the temperature and density distributions. The temperature sharply increases with time from 4400 K to above 9400 K in Case I without the radiative cooling effect. Such a temperature increase is too large to match the measured temperature increase in a typical EB ($\sim 600\text{--}3000$ K) (e.g., Georgoulis et al. 2002; Fang et al. 2006; Hong et al. 2017). The temperature increase becomes slower and slower in Case II and Case III after plasmoid instability appears, and the maximum temperature stays at about 7000 K in Case II and 6800 K in Case III, eventually. Therefore, the temperature increases in Case II and Case III are in good agreement with that in a typical EB. The slightly higher temperature in Case II indicates that the Carlsson & Leenaarts (2012) radiative cooling model is stronger than the Gan & Fang (1990) model. Figure 2 also shows that the strong radiative cooling results in the more non-uniform density distributions inside the plasmoids, and the maximum density in Case III is much higher than that in Case I at $t = 70.32$ s. In Figure 3(b) and (c), we can also see that the radiative cooling efficiently accelerates the outflow velocity and increases the reconnection rate to a higher value during the later stage. The maximum outflow velocity in Case III stays around 9 km s^{-1} , which is consistent with the inverted outflow velocity of a chromospheric reconnection event based on the observational results (Díaz Baso et al. 2021).

As we know, the thermal energy equation in the MHD model is stated as below:

$$\begin{aligned} \frac{de_{\text{th}}}{dt} = & -p\nabla \cdot \mathbf{v} + \frac{1}{2\xi}\text{tr}(\tau_s^2) \\ & + \frac{\eta}{\mu}|\nabla \times \mathbf{B}|^2 + \frac{\eta_{\text{AD}}}{\mu^2}|\mathbf{B} \times (\nabla \times \mathbf{B})|^2 \\ & + Q_{\text{rad}}, \end{aligned} \quad (25)$$

where e_{th} is the thermal energy density and the ‘‘tr’’ in the second term on the right-hand side means evaluating the trace of a matrix. Figure 4 shows the evolutions of the average power densities contributed by different terms on the right-hand side

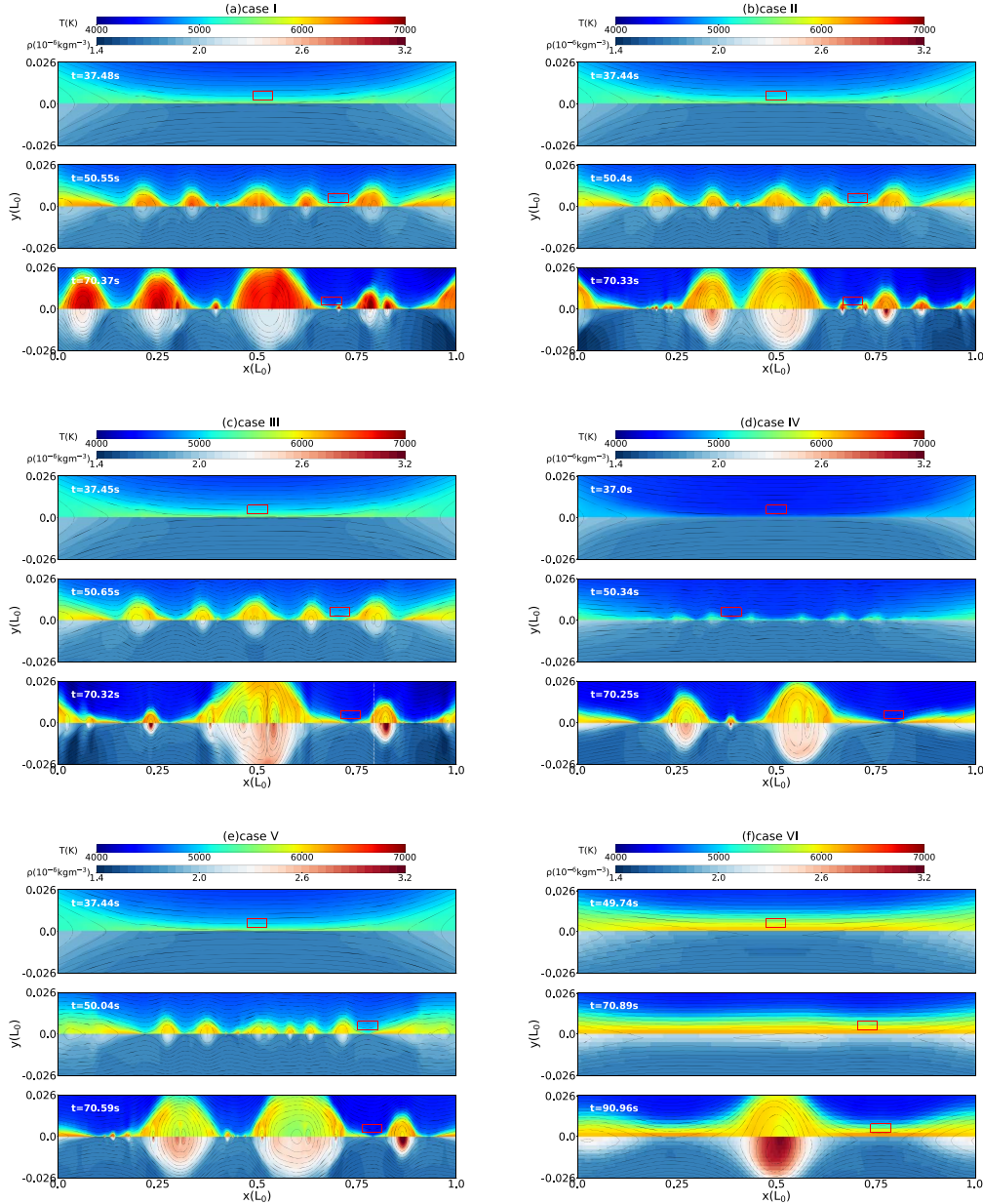


Figure 2. The 2D distributions of temperature and plasma density at three typical times in six different cases. The two different background colors in half of the upper and lower panels correspond to the temperature and density, respectively. The black solid lines represent the magnetic field lines.

of Equation (25) in different cases. Variables Q_{comp} , Q_{vis} , Q_{ei} , Q_{en} , Q_{Amp} and Q_{rad} are the average power densities of the compression heating, heating caused by the viscosity ξ , Joule heating contributed by magnetic diffusions η_{ei} and η_{en} , heating contributed by the ambipolar diffusion η_{AD} and lost thermal energy by the radiative cooling effect, respectively. They are the average values calculated in the area of the main reconnection region within $-0.026L_0 \leq y \leq 0.026L_0$ and $0 \leq x \leq L_0$. We should point out that the compression heating Q_{comp} has been calculated by using the average values of both

$\mathbf{v} \cdot \nabla p$ and $-p \nabla \cdot \mathbf{v}$ in the main reconnection region, because $Q_{\text{comp}} = \int_0^t \int \mathbf{v} \cdot \nabla p \, dF dt = \int_0^t \int -p \nabla \cdot \mathbf{v} \, dF dt$ (Birn et al. 2012), where $\int dF$ represents the integration in the x and y directions.

Comparing the results in Figure 4(a), (b) and (c), one can find that the evolutions of different heating terms are very similar in Cases I, II and III. Q_{en} is larger than the other heating terms during the early reconnection stage. However, Q_{en} sharply decreases to a much lower value after plasmoid

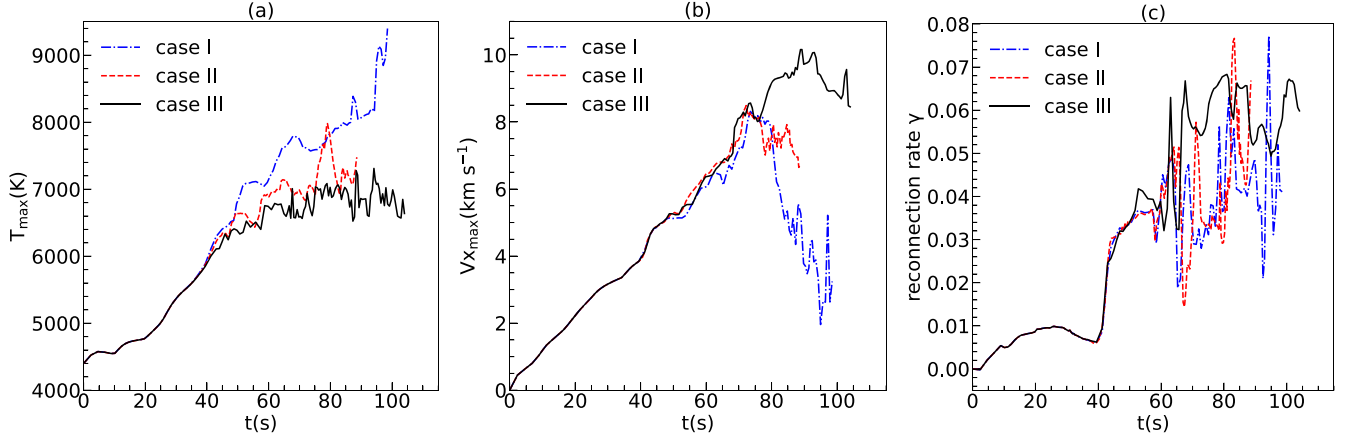


Figure 3. The time evolutions of the maximum temperature T_{\max} (a), the maximum outflow velocity in the x -direction $v_{x,\max}$ (b), and the reconnection rate γ in Cases I, II and III.

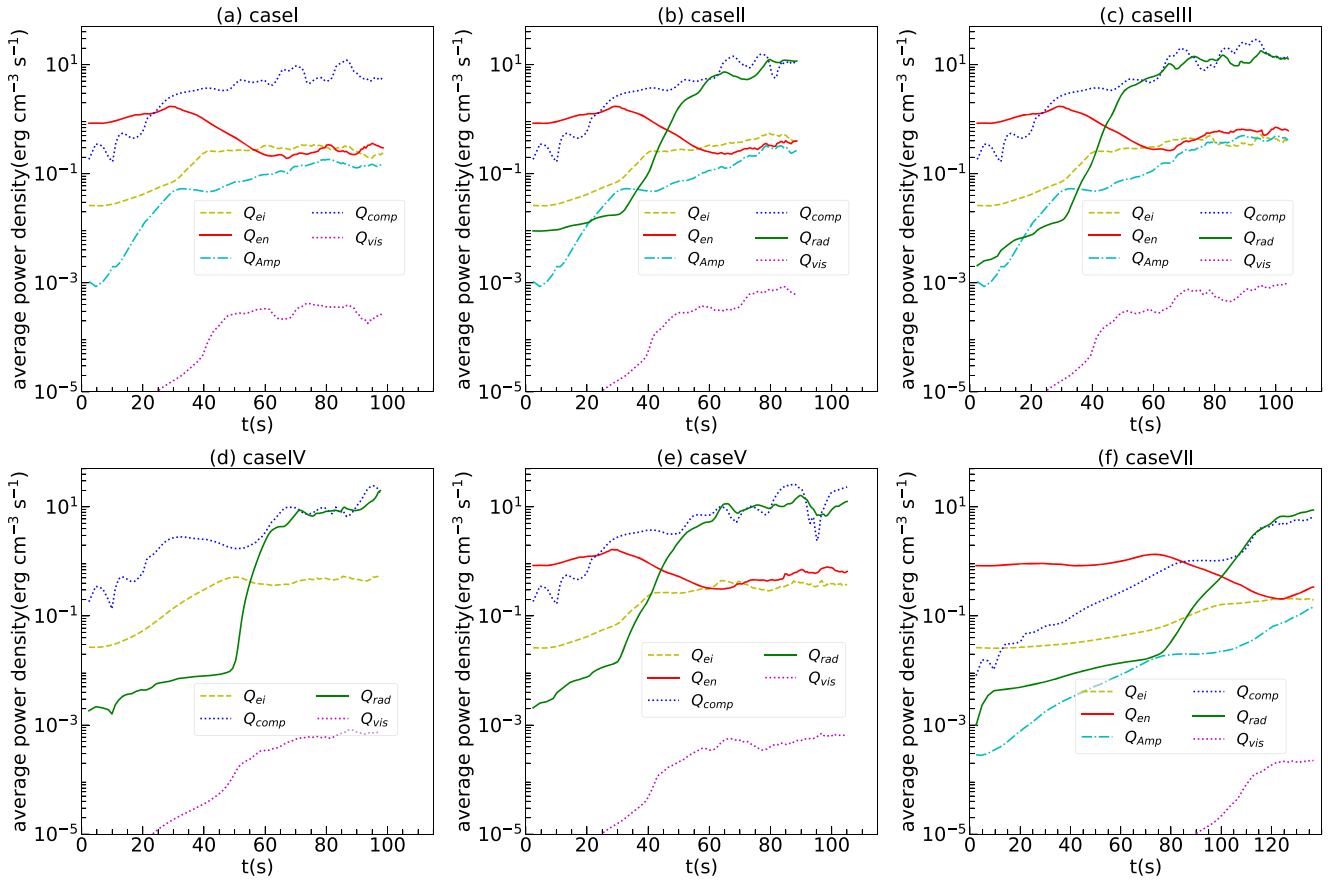


Figure 4. The time evolutions of the average power density contributed by different heating terms and the radiative cooling in six different cases.

instability appears, but the general trends of all the other terms increase with time. Eventually, Q_{comp} dominates over the other terms, Q_{en} decreases to a value with the same order of magnitude as Q_{ei} and Q_{Amp} , and Q_{vis} is always much smaller

than the other terms and can be ignored in all the cases. When we look into the details, we can find the differences among the three cases. The value of Q_{comp} in Case III reaches above $10 \text{ erg cm}^{-3} \text{ s}^{-1}$, while this value is smaller than

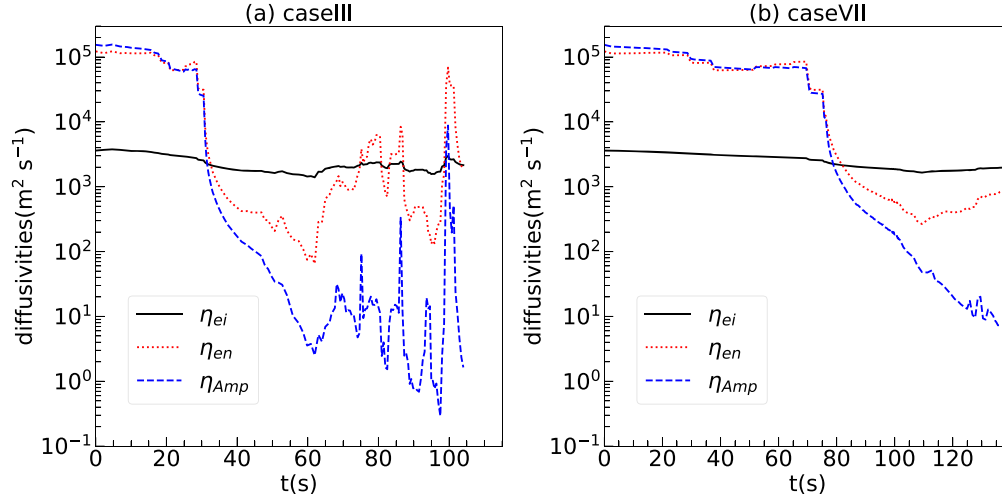


Figure 5. The time evolutions of the different diffusion coefficients (η_{ei} , η_{en} and η_{Amp}) at the main reconnection X-point in Case III and Case VII.

$10 \text{ erg cm}^{-3} \text{ s}^{-1}$ in Case I. The lower temperature in Case III also makes the values of Q_{cn} , Q_{Amp} and Q_{ei} in Case III be higher than those in Case I. Therefore, the radiative cooling effect efficiently promotes the generation of more thermal energy. As demonstrated in Figure 4(b) and (c), the radiative cooling effect is much weaker than total heating effect before plasmoid instability appears in both Case II and Case III. After that, the radiative cooling term Q_{rad} sharply increases, and then it gradually becomes stable after $t = 60 \text{ s}$ in both cases. The radiative cooling effect has been increased by four orders of magnitude during the whole reconnection process of 100 s. The final average power density of the radiative cooling term Q_{rad} is also $\sim 10 \text{ erg cm}^{-3} \text{ s}^{-1}$ in both cases, and the radiative losses at the reconnection site are then calculated as $L_{rad} = Q_{rad} \times L_0 = 200 \text{ kW m}^{-2}$, which is very close to the calculated radiative loss (160 kW m^{-2}) of the chromospheric reconnection event based on the observational results (Díaz Baso et al. 2021).

3.2. Results with Different Diffusions

The collisions between different kinds of particles in EBs are also strong because of the high plasma density there. Such strong collisions might efficiently affect the magnetic reconnection process through the different diffusion terms in the energy equation, Equation (3), and the magnetic induction equation, Equation (4). Figure 5 displays the time-dependent diffusivities at the main reconnection X-point inside the current sheet. In order to unify the units of three diffusion coefficients, we evaluate the ambipolar diffusion via $\eta_{Amp} = B^2 \eta_{AD} / \mu_0$. As shown in Figure 5, the magnetic diffusivity contributed by electron-neutral collision η_{en} and the ambipolar diffusion coefficient η_{Amp} are above $10^5 \text{ m}^2 \text{ s}^{-1}$ at the beginning, and they are almost two orders of magnitude higher than the

magnetic diffusivity contributed by electron-ion collision η_{ei} . However, η_{en} and η_{Amp} at the main reconnection X-point sharply decrease during the reconnection process because of the increasing temperature and ionization degree; they decrease to a value that is smaller than η_{ei} during the later stage. Therefore, it is necessary to detailedly check how these time dependent diffusivities affect the whole reconnection process. The results in Cases III, IV, V and VI are compared to check the effects of different diffusions. We only include the η_{ei} term in Case IV, but we include both the η_{ei} and η_{en} terms in Case V. The terms related to the ambipolar diffusion η_{AD} are turned off in both Case IV and Case V. Though all the diffusion terms are included in Case VI, the limited resolution causes the numerical diffusion in Case VI to be much larger than the three physical diffusions.

The 2D distributions of the temperature and plasma density at three different times in Cases III, IV, V and VI are presented in Figure 2(c), (d), (e) and (f), respectively. The time evolutions of the maximum temperature T_{max} , maximum velocity in the x -direction v_{xmax} and reconnection rate γ in the four cases are presented in Figure 6. Comparing Figure 2(c) and (e), we can find that the missing ambipolar diffusion effect slightly changes the evolutions of the plasmoid instability; the plasmoids appear a little bit later and they are slightly smaller in Case V than those in Case III at the same point in time. As shown in Figure 6, the time evolutions of T_{max} , v_{xmax} and γ are very similar in Case III and Case V. These results indicate that the ambipolar diffusion is not important in such a reconnection process. Comparing Figure 2(d) and (e), one can clearly see that the missing η_{en} terms cause strong influences on the reconnection process. Before $t = 60 \text{ s}$, the temperature inside the current sheet in Case IV is much lower than that in Case III, and the plasmoids appear about 5 s later in Case IV. The missing η_{en} terms in Case IV also result in the smaller outflow

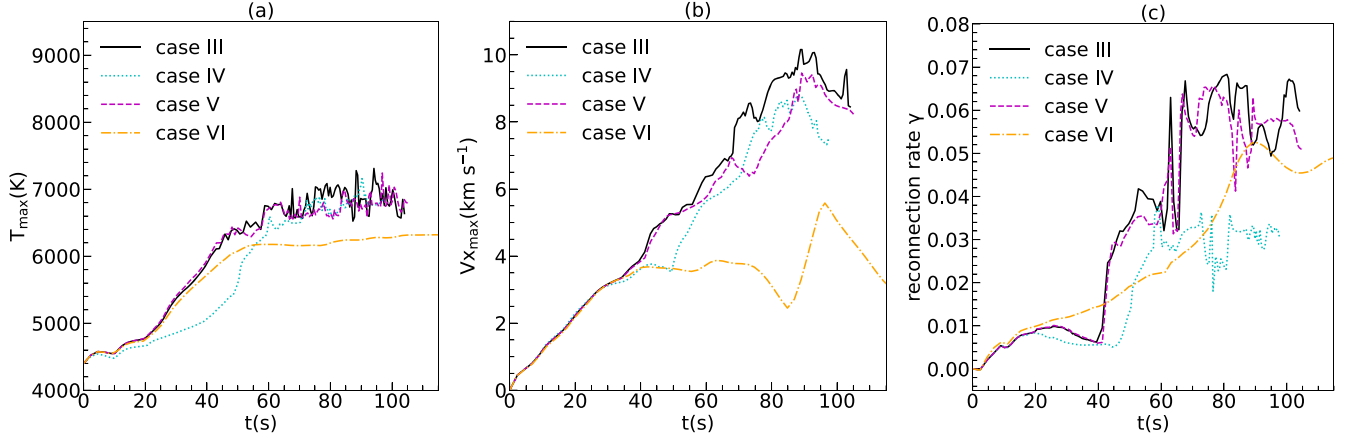


Figure 6. The time evolutions of the maximum temperature T_{\max} (a), the maximum outflow velocity in the x -direction $v_{x\max}$ (b), and the reconnection rate γ in Cases III, IV, V and VI.

velocity $v_{x\max}$ and smaller reconnection rate γ as displayed in Figure 6(b) and (c). These results indicate that the magnetic diffusion caused by the electron-neutral collision plays an important role in the magnetic reconnection process of an EB.

Figures 2(f) and 6 show that the large numerical diffusion in Case VI makes the evolution of the whole reconnection process be very different. The plasmoids appear much later and much fewer plasmoids appear in this case. The temperature increase and reconnection outflow velocity are also strongly underestimated in Case VI. Therefore, the realistic physical diffusions and high resolutions in numerical simulations are very necessary for investigating the reconnection and heating mechanisms in EBs.

4. Discussion

4.1. Mechanisms Leading to Fast Magnetic Reconnection

The high plasma density in EBs makes the collisions between different kinds of particles and the radiative cooling effect be strong in the magnetic reconnection region. The strong collisions will lead to the large diffusion terms in the energy equation, Equation (3), and the magnetic induction equation, Equation (4). The strong radiative cooling will also affect the evolution of the energy equation, Equation (3).

Previous theoretical results (Brandenburg & Zweibel 1994) demonstrated that the ambipolar diffusion caused by the decoupling of ions and neutrals can result in a thinner current sheet and much higher reconnection rate when there is no guide field. Theoretical work in Uzdensky et al. (2010) indicated that the strong radiative cooling can also accelerate the reconnection when the guide field vanishes. The 2D numerical results in Ni et al. (2015) then demonstrated that the ambipolar diffusion and radiative cooling indeed make the thinning of the current sheet faster and the reconnection rate higher before plasmoid instability appears, in the case with zero guide field. However,

the reconnection rate always sharply increased to a value ~ 0.02 – 0.03 after plasmoid instability appears (Ni et al. 2015), no matter whether the ambipolar diffusion and radiative cooling effects are included in the simulations or not.

Figures 3(c) and 6(c) show the time evolutions of the reconnection rate in different cases. We can see that the reconnection rate is smaller than 0.01 before plasmoid instability appears. After $t = 25$ s, the reconnection rate decreases to an even lower value. The reason is that the reconnection rate γ scales with the Lundquist number S as $\gamma \sim S^{-1/2}$ in the earlier quasi-steady stage with the Sweet-Parker like current sheet, where $S = Lv_A/\eta$. The decreasing η as shown in Figure 5 causes the decreasing reconnection rate during this stage. After plasmoid instability appears, the reconnection rate is always sharply increased in all the cases, which is consistent with the previous simulations (Ni et al. 2015; Ni & Lukin 2018). However, there are some differences between this work and the previous one (Ni et al. 2015). Comparing the results in Case I and Case III, we can see that the strong radiative cooling effect still slightly increases the reconnection rate after plasmoid instability appears. The results in Figure 6(c) demonstrate that η_{en} also plays an important role that results in the fast magnetic reconnection; the reconnection rates in Case III and Case V are about two times larger than that in Case IV, even after plasmoid instability appears. Since η_{en} is about 25 times larger than η_{ei} before $t = 30$ s in Case III, the reconnection rate in Case III is expected to be about 5 times higher than that in Case IV without η_{en} during this stage. However, the reconnection rate in Case III is only slightly higher than that in Case IV as shown in Figure 6(c). The reason is that the AMR level is smaller than 4 before $t = 30$ s, which causes the low resolution during this stage. The low resolution then results in the high numerical diffusion, and the reconnection rate in Case IV is overestimated during this stage. The similar results in Case III and Case V demonstrate that the

ambipolar diffusion effect can be ignored in the whole reconnection process.

In order to confirm these results and conclusions, we have calculated the reconnection rate in larger boxes in the upstream region around the main reconnection X-point. The derived reconnection rate in the larger box is relatively lower but the whole evolution trend is the same as those shown in Figures 3(c) and 6(c). The reconnection rate at the main-X point is also calculated based on the values of ηJ_z (Leake et al. 2012, 2013; Ni & Lukin 2018), which exhibits larger fluctuations than the results presented in Figures 3(c) and 6(c) after plasmoid instability appears. However, the main conclusions are still not changed.

Our numerical results indicate that both the large magnetic diffusion caused by electron-neutral collisions and the plasmoid instability can lead to fast magnetic reconnection in an EB-like event. The strong radiative cooling in EBs can also accelerate magnetic reconnection even when the strong guide field is included. However, we should point out that the research about the ion recombination effect on magnetic reconnection (Leake et al. 2012, 2013) in the EB-like event is outside the scope of this work.

4.2. Heating Mechanisms

Though magnetic reconnection is believed to be the main mechanism accounting for EBs, the energy converting mechanism inside the reconnection diffusion region is still not well understood. The high resolution MHD simulations with time dependent ionization degree, more realistic diffusions and radiative cooling model allow us to deeply analyze the heating mechanisms in EBs.

Figure 4 plots the time evolutions of the average power density contributed by different heating terms in the thermal energy equation, Equation (25). The results in Case III show that the Joule heating contributed by electron-neutral collision (Q_{en}) is larger than the other heating terms during the early reconnection stage. After plasmoid instability appears, Q_{en} sharply decreases to a much lower value, but the general trends of all the other terms increase with time. The compression heating Q_{comp} exceeds the Joule heating Q_{en} after 25 s. Eventually, Q_{en} decreases to $\sim 0.4 \text{ erg cm}^{-3} \text{ s}$, Q_{ei} and Q_{Amp} increase to a value with the same order of magnitude as Q_{en} , and Q_{comp} increases to a value above $\sim 10 \text{ erg cm}^{-3} \text{ s}$. The numerical results in Case VII show similar behaviors as those in Case III. However, the five times smaller initial perturbation in Case VII causes the slower evolution of the current sheet and the plasmoids appear much later. In Case VII, Q_{en} is much larger than Q_{comp} and the Joule heating caused by η_{en} is the most important heating term before plasmoid instability appears. Then, the compression heating Q_{comp} increases and exceeds the Joule heating Q_{en} after plasmoid instability appears ($\sim 90 \text{ s}$). We can expect that Q_{comp} will also increase to a value

with $Q = 10 \text{ erg cm}^{-3} \text{ s}$ in Case VII during the later stage. When such a turbulent reconnection process happens in an EB with the typical size of $V = 700 \times 700 \times 700 \text{ km}^3$ and the lifetime of $t = 5 \text{ minutes}$, the total thermal energy supplied by magnetic reconnection is $E = Q \times V \times t \simeq 10^{27} \text{ erg}$, which is in the energy range of a typical EB ($\sim 10^{25} - 10^{28} \text{ erg}$) measured from observations (e.g., Georgoulis et al. 2002; Fang et al. 2006).

The numerical results indicate that the sharp increase of the compression heating is triggered by the appearance of the plasmoids. The compression heating always dominates to supply the thermal energy in EBs as long as the turbulent reconnection mediated by plasmoids appears. As affirmed in Figure 2, the interactions and coalescence of the plasmoids can strongly enhance the local compression inside the plasmoids, many slow-mode and fast-mode shocks appear (Ni et al. 2015, 2016, 2022), and the kinetic energy generated in the reconnection process is then converted into thermal energy in this process (Ni et al. 2022). Figure 7(a) presents the divergence of the velocity in a plasmoid shown in Figure 2(c); the large compressions appear in the regions with obvious blue and red colors. The vertical white dash-dotted line in Figure 7(a) is the same line as drawn in Figure 2(c). The two fast-mode shock fronts are located at around the two heads of the plasmoid with blue colors. The vertical white dash-dotted line crosses a pair of slow-mode shock fronts with red colors. Figure 7(b) plots the distributions of ρ/ρ_{max} , T/T_{max} and p/p_{max} along the vertical white dash-dotted line. The results in Figure 7(b) demonstrate that the variables suddenly increase to higher values around the two slow-mode shock fronts. Figure 7(c) displays the time evolutions of Q_{comp} and Q_{kin} , where Q_{kin} is the average power density of the kinetic energy calculated inside the reconnection region within $-0.026L_0 \leq x \leq 0.026L_0$ and $0 \leq y \leq L_0$. We can see that the sharp increase of Q_{comp} always corresponds to the sharp decrease of Q_{kin} . Since the small shock structures inside the plasmoids strongly vary with time and location and the other compression heating processes always combine with shocks at the same time, it is difficult to evaluate how much thermal energy is converted from kinetic energy only via shocks.

Such a result is different from the previous work in Ni et al. (2016), which showed that Joule heating dominates to heat the plasmas in the magnetic reconnection process in EBs with a similar plasma β as in this work. However, we should point out that the fixed ionization degree caused magnetic diffusion contributed by electron-neutral collision and ambipolar diffusion to be overestimated, and the radiative cooling process was underestimated in the reconnection region in Ni et al. (2016). Therefore, the Joule heating and temperature increase were overestimated in Ni et al. (2016). The current model in this work has been improved significantly by including the time dependent ionization degree of hydrogen and helium, and a

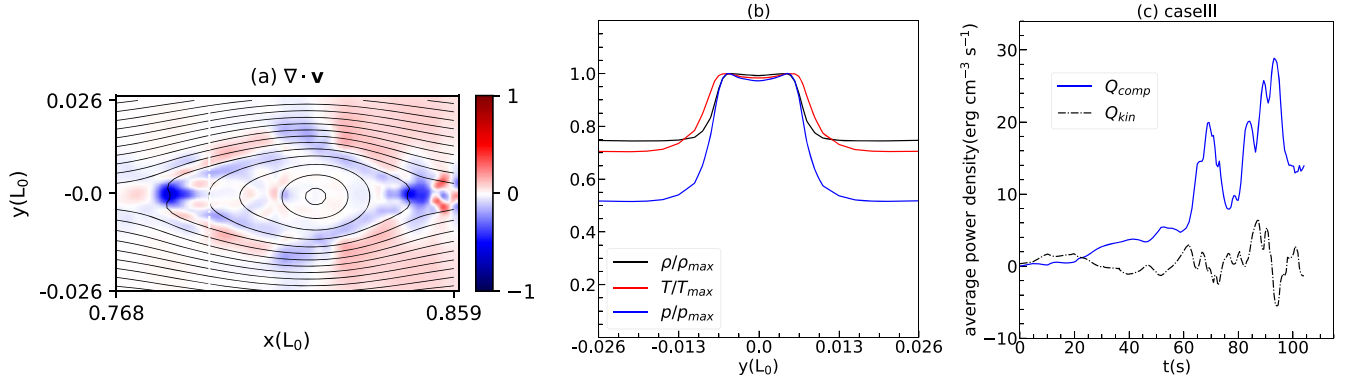


Figure 7. (a) The divergence of the velocity in a plasmoid shown in Figure 2(c); the vertical white dash-dotted line is the same line as drawn in Figure 2(c). (b) The distributions of ρ/ρ_{max} , T/T_{max} and p/p_{max} along the vertical white dash-dotted line in (a), where ρ_{max} , T_{max} and p_{max} are the maximum values of mass density, temperature and pressure along this line respectively. (c) The time evolutions of Q_{comp} and Q_{kin} , where Q_{comp} and Q_{kin} are the average power densities of the compression heating and kinetic energy, respectively.

more realist radiative cooling model. In addition, the coalescence of the plasmoids lasts for a longer time to form much bigger plasmoids in this work, which lead to a larger compression heating effect. Recently, Ni et al. (2022) studied the low β magnetic reconnection process in ultraviolet bursts based on the same MHD model as in this work, and the main difference between the current model in this work and the one in Ni et al. (2022) is the magnetic field strength, and hence the plasma β . Their results demonstrated that the thermal energy accounting for ultraviolet bursts around the solar TMR is also mainly supplied by the local compression heating triggered by plasmoid instability. The much lower plasma β in Ni et al. (2022) leads to the much stronger compression heating effect. Therefore, we can conclude that such a mechanism plays an important role for different kinds of local heating events related to magnetic reconnection in the low solar atmosphere.

However, we should point out that the plasmoid instability might not always appear in the EB-like events, or in the whole stage of the EB events. Then, the Joule heating contributed by η_{en} (the magnetic diffusion caused by electron-neutral collision) will play the most important role for supplying thermal energy in a lower temperature EB with a quasi-steady state reconnection process.

5. Conclusions and Outlooks

In this work, we have studied the reconnection and heating mechanisms in EBs based on a single-fluid 2.5D MHD framework. Compared with previous works (Ni et al. 2015, 2016, 2021), the time dependent ionization degrees of hydrogen and helium are included to result in more realistic diffusivities and viscosity, and two improved radiative cooling models have been applied in the simulations. The reconnection

current sheet is assumed to be located around the solar TMR with the initial temperature of 4400 K and density of $1.66057 \times 10^{-6} \text{ kg m}^{-3}$. We have tested seven different cases to study the effects of radiative cooling, different diffusions, initial perturbations and resolutions on magnetic reconnection. The main conclusions are summarized as below:

1. In the weakly ionized plasmas around the solar TMR, the reconnection rate is smaller than 0.01 and decreases with time during the quasi-steady state Sweet-Parker like current sheet stage, then sharply increases to a value higher than 0.05 during the later unstable reconnection stage with plasmoid instability. Both the large value of η_{en} and plasmoid instability contribute to the fast magnetic reconnection in an EB-like event.
2. The compression heating always dominates to supply thermal energy in EBs as long as turbulent reconnection mediated by plasmoids appears. The local compression heating in the reconnection region was efficiently enhanced when the plasmoids collide and coalescence with each other, and part of the generated kinetic energy is converted to thermal energy during this process. However, the Joule heating contributed by η_{en} can play a major role to heat plasmas when magnetic reconnection in EBs is during the quasi-steady stage with smaller temperature increases.
3. The average power density caused by the compression heating can reach above $10 \text{ erg cm}^{-3} \text{ s}$, which can supply a total energy of 10^{27} erg for an EB with size of $1''$ and lifetime of 5 min. The strong radiative cooling in EBs results in radiative loss at the reconnection site being 200 kW m^{-2} , which is close to the measured radiative

loss (160 kW m^{-2}) of the observed chromospheric reconnection event (Díaz Baso et al. 2021).

4. The strong radiative cooling effect in the reconnection region constrains the temperature increase to a reasonable value ($\sim 2400 \text{ K}$), which is consistent with the results based on semi-empirical models and numerous spectral analyses from observations (e.g., Georgoulis et al. 2002; Fang et al. 2006; Hong et al. 2017). The radiative cooling effect also promotes the generation of more thermal energy, accelerates the outflow velocity and increases the reconnection rate.

Previous two-fluid MHD simulations showed that the ion recombination effect can result in fast magnetic reconnection in weakly ionized plasmas (Leake et al. 2012, 2013). Future multi-fluid MHD simulations with a more realistic radiative cooling model is still necessary to study the magnetic reconnection process in EBs. The recent 3D radiation magnetohydrodynamics (RMHD) simulations have successively simulated the formation of EBs in the photosphere and synthesized $H\alpha$ images and spectral line profiles (Danilovic et al. 2017; Danilovic 2017). However, these 3D RMHD simulations always showed a single X-point structure inside the reconnection region. The high resolution observational results indicate that EBs might include many fine structures (Hashimoto et al. 2010; Díaz Baso et al. 2021), and the recent 3D MHD simulations also demonstrated that a small scale flux rope (corresponding to the plasmoid in 2D) can be generated in the reconnection process of an EB (Cheng et al. 2021). Therefore, future higher resolution 3D RMHD simulations with more realistic diffusions are very important to reveal the magnetic reconnection and heating mechanism, and the fine structures inside an EB. The higher resolution and more precise observational results from the Daniel K. Inouye Solar Telescope (DKIST) (Rast et al. 2021), Chinese H-Alpha Solar Explorer (CHASE) (Li et al. 2022) and other telescopes should be combined with simulations to reveal the hidden smaller scale physics in EBs.

Acknowledgments

This research is supported by the National Key R&D Program of China No. 2022YFF0503800; the National Natural Science Foundation of China (NSFC, Grant Nos. 11973083 and 11933009); the Strategic Priority Research Program of CAS with grants XDA17040507; the outstanding member of the Youth Innovation Promotion Association CAS (No. Y2021024); the Applied Basic Research of Yunnan Province in China Grant 2018FB009; the Yunling Talent Project for the Youth; the project of the Group for Innovation of Yunnan Province grant 2018HC023; the Yunling Scholar Project of the Yunnan Province and the Yunnan Province Scientist Workshop of Solar Physics; Yunnan Key Laboratory of Solar Physics and

Space Exploration (No. 202205AG070009). The numerical calculations and data analysis were done at the Hefei Advanced Computing Center and the Computational Solar Physics Laboratory of Yunnan Observatories.

References

- Archontis, V., & Hood, A. W. 2009, *A&A*, 508, 1469
 Avrett, E. H., & Loeser, R. 2008, *ApJS*, 175, 229
 Barata, J. A. S., & Conde, C. A. N. 2010, *NIMPA*, 619, 21
 Berghmans, D., Auchère, F., Long, D., et al. 2021, *A&A*, 656, 11
 Birn, J., Borovsky, J. E., & Hesse, M. 2012, *PhPI*, 19, 082109
 Brandenburg, A., & Zweibel, E. G. 1994, *ApJL*, 427, L91
 Carlsson, M., & Leenaarts, J. 2012, *A&A*, 539, A39
 Chae, J., & Litvinenko, Y. E. 2021, *RAA*, 21, 2
 Chen, P.-F., Fang, C., & Ding, M.-D. 2001, *ChJAA*, 1, 176
 Chen, Y., Przybylski, D., Peter, H., et al. 2021, *A&A*, 656, 12
 Chen, Y., Tian, H., Zhu, X., et al. 2019, *Science China Technological Sciences*, 62, 1555
 Cheng, G.-C., Ni, L., Chen, Y.-J., Ziegler, U., & Lin, J. 2021, *RAA*, 21, 229
 Danilovic, S. 2017, *A&A*, 601, A122
 Danilovic, S., Solanki, S. K., Barthol, P., et al. 2017, *ApJS*, 229, 5
 dePontieu, B., McIntosh, S., Hansteen, V. H., et al. 2007, *PASJ*, 59, S655
 Díaz Baso, C. J., de la Cruz Rodríguez, J., & Leenaarts, J. 2021, *A&A*, 647, A188
 Ding, M. D., Henoux, J. C., & Fang, C. 1998, *A&A*, 332, 761
 Ellerman, F. 1917, *ApJ*, 46, 298
 Fang, C., Tang, Y. H., Xu, Z., Ding, M. D., & Chen, P. F. 2006, *ApJ*, 643, 1325
 Gan, W. Q., & Fang, C. 1990, *ApJ*, 358, 328
 Georgoulis, M. K., Rust, D. M., Bernasconi, P. N., & Schmieder, B. 2002, *ApJ*, 575, 506
 Hashimoto, Y., Kitai, R., Ichimoto, K., et al. 2010, *PASJ*, 62, 879
 Hong, J., Ding, M. D., & Cao, W. 2017, *ApJ*, 838, 101
 Hong, J., Li, Y., Ding, M. D., & Hao, Q. 2021, *ApJ*, 921, 50
 Huang, Z., Li, B., & Xia, L. 2019, *STP*, 5, 58
 Isobe, H., Tripathi, D., & Archontis, V. 2007, *ApJL*, 657, L53
 Ji, H., Daughton, W., Jara-Almonte, J., et al. 2022, *NatRP*, 4, 263
 Joshi, J., & Rouppe van der Voort, L. H. M. 2022, *A&A*, 664, A72
 Joshi, R., Schmieder, B., Tei, A., et al. 2021, *A&A*, 645, A80
 Leake, J. E., Lukin, V. S., & Linton, M. G. 2013, *PhPI*, 20, 061202
 Leake, J. E., Lukin, V. S., Linton, M. G., & Meier, E. T. 2012, *ApJ*, 760, 109
 Li, C., Fang, C., Li, Z., et al. 2022, *SCPMA*, 65, 289602
 Li, Z., Fang, C., Guo, Y., et al. 2015, *RAA*, 15, 1513
 Murphy, N. A., & Lukin, V. S. 2015, *ApJ*, 805, 134
 Murtas, G., Hillier, A., & Snow, B. 2021, *PhPI*, 28, 032901
 Murtas, G., Hillier, A., & Snow, B. 2022, *PhPI*, 29, 062302
 Ni, L., Chen, Y., Peter, H., Tian, H., & Lin, J. 2021, *A&A*, 646, A88
 Ni, L., Cheng, G., & Lin, J. 2022, *A&A*, 665, A116
 Ni, L., Ji, H., Murphy, N. A., & Jara-Almonte, J. 2020, *RSPSA*, 476, 20190867
 Ni, L., Kliem, B., Lin, J., & Wu, N. 2015, *ApJ*, 799, 79
 Ni, L., Lin, J., Rousev, I. I., & Schmieder, B. 2016, *ApJ*, 832, 195
 Ni, L., & Lukin, V. S. 2018, *ApJ*, 868, 10
 Pariat, E., Aulanier, G., Schmieder, B., et al. 2004, *ApJ*, 614, 1099
 Pariat, E., Schmieder, B., Berlicki, A., et al. 2007, *A&A*, 473, 279
 Parnell, C., & Jupp, P. 2000, *ApJ*, 529, 554
 Peter, H., Tian, H., Curdt, W., et al. 2014, *Sci*, 346, 1255726
 Rast, M. P., Bello González, N., Bellot Rubio, L., et al. 2021, *SoPh*, 296, 70
 Rutten, R. J. 2003, *Radiative Transfer in Stellar Atmospheres* (Lecture Notes Utrecht Univ.)
 Samanta, T., Tian, H., Yurchyshyn, V., et al. 2019, *Sci*, 366, 890
 Schmieder, B., Joshi, R., & Chandra, R. 2022, *AdSpR*, 70, 1580
 Shen, Y. 2021, *RSPSA*, 477, 217
 Singh, K., Sakaue, T., Nakamura, N., et al. 2019, *ApJ*, 884, 15
 Song, Y., Tian, H., Zhu, X., et al. 2020, *ApJL*, 893, L13
 Tian, H., Xu, Z., He, J., & Madsen, C. 2016, *ApJ*, 824, 96

- Uzdensky, D. A., Loureiro, N. F., & Schekochihin, A. A. 2010, [PhRvL](#), **105**, 235002
- Vernazza, J. E., Avrett, E. H., & Loeser, R. 1981, [ApJS](#), **45**, 635
- Vissers, G. J. M., Rouppe van der Voort, L. H. M., & Rutten, R. J. 2013, [ApJ](#), **774**, 32
- Vissers, G. J. M., Rouppe van der Voort, L. H. M., Rutten, R. J., Carlsson, M., & De Pontieu, B. 2015, [ApJ](#), **812**, 11
- Vranjes, J., & Krstic, P. S. 2013, [A&A](#), **554**, A22
- Wang, J. 1995, [ScChA](#), **38**, 853
- Xu, X.-Y., Fang, C., Ding, M.-D., & Gao, D.-H. 2011, [RAA](#), **11**, 225
- Xue, Z., Yan, X., Yang, L., et al. 2021, [ApJL](#), **919**, L29
- Ziegler, U. 2008, [CoPhC](#), **179**, 227
- Ziegler, U. 2011, [JCoPh](#), **230**, 1035